

3D-FDTD Modeling of Angular Spread for the Extraordinary Transmission Spectra of Metal Films with Arrays of Subwavelength Holes

Joseph M. Heer · James V. Coe

Received: 11 May 2011 / Accepted: 3 August 2011
© Springer Science+Business Media, LLC 2011

Abstract Extraordinary transmission through a metal film with an array of subwavelength holes (mesh) can be modeled effectively using three-dimensional finite difference time domain (3D-FDTD) calculations. A simple 3D-FDTD model, where a plane wave of light at perpendicular incidence with no angular spread interacts with a periodic repeating mesh, models the shape and location of the transmission resonance peaks qualitatively but not quantitatively. The simple 3D-FDTD model gives peaks that are tall, sharp, and red-shifted compared to experimental measurements using a benchtop Fourier transform infrared (FTIR) spectrometer. It was discovered that the simple model does not account accurately for diffraction order scattering by the mesh or the angular spread of the actual FTIR beam. This work describes a more sophisticated model that accounts for these factors and agrees quantitatively with experimental FTIR results.

Keywords Metal films with hole arrays · Extraordinary transmission · FDTD modeling · Plasmonic metal films · Infrared transmission

Introduction

Plasmonic nickel mesh (metal film with an array of subwavelength holes) has been used by us to study the infrared spectra and resonance shifting by coatings [1, 2] and particles placed on the mesh [3–5]. Our plasmonic

nickel mesh (Precision Eforming, Courtland, NY, www.precisionforming.com) has square holes (about $5 \times 5 \mu\text{m}$) in a square lattice pattern ($L=12.7\text{-}\mu\text{m}$ lattice parameter), with a thickness of $\sim 2 \mu\text{m}$ (see inset of Fig. 1). An experimental, perpendicular incidence, zero-order transmission spectrum of this physical mesh using a benchtop Fourier transform infrared (FTIR) spectrometer is shown in Fig. 1 (less intense trace labeled “Experiment”). A simple, three-dimensional, finite difference time domain (3D-FDTD) simulation of the same mesh with light at perpendicular incidence ($k_x=0.0$) is also shown in Fig. 1 (top trace labeled FDTD) [6]. Modeling and experimental details are explained later in “3D-FDTD Method.” A number of FDTD studies of mesh [6–20] show the feasibility of the FDTD approach as a way to model resonant transmission through plasmonic mesh structures, so the dramatic differences between the FDTD model spectrum and the experimental spectrum shown in Fig. 1 are surprising to the uninitiated. The simple FDTD model places the primary resonance at about the right place, but the model results show important differences from the experiment: (1) peaks are much taller and narrower than the experiment, (2) the primary resonance is shifted to a lower frequency range, (3) transmission drops to zero at several points in the model spectrum, but never does so in the experimental spectrum, and (4) in general, the model features are sharper and less smoothed.

The periodic structure of the mesh scatters transmitted light into distinct, well-defined diffraction spots. The benchtop FTIR spectrometer used in the physical experiment was only capable of detecting the zero-order diffraction spot due to the size of the detector window and the spectrometer optics. On the other hand, due to the periodic boundary conditions in the simple, periodic 3D-FDTD model, all orders of scattered light were detected, including

J. M. Heer · J. V. Coe (✉)
Department of Chemistry, The Ohio State University,
100 West 18th Avenue,
Columbus, OH 43210-1173, USA
e-mail: coe.1@osu.edu

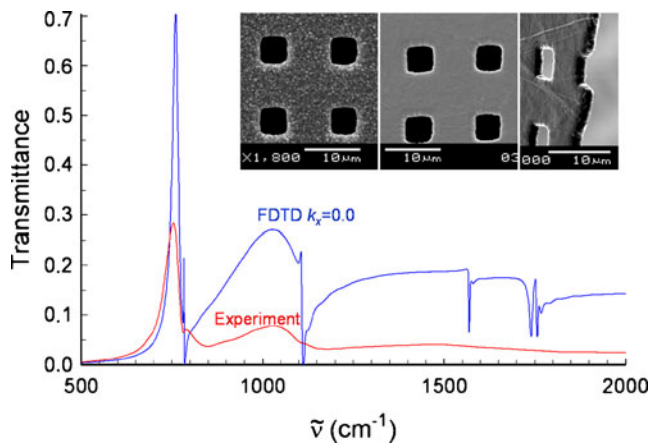


Fig. 1 The lower trace (experiment) is the experimental transmittance of the Ni mesh pictured in the inset as measured with a benchtop FTIR spectrometer at perpendicular incidence in zero order. The upper trace (FDTD) is a simple 3D-FDTD simulation of the transmittance at perpendicular incidence with all diffraction orders and no angular spread. Inset is a scanning electron microscope image of the Ni mesh which has square holes of 5- μm width, a square lattice with a 12.7- μm lattice parameter, and ~ 2 - μm width. The bars indicate 10 μm

those at very high scattering angles. Limiting the model results to *only* the zero-order contribution brought the peak intensities in the model much closer to the experimental results for the higher frequency resonance peaks, but had no effect on the large discrepancy at the low-frequency primary resonance peak. The angular spread of the incoming light beam due to spectrometer optics, first thought to be negligible and unimportant, turns out to be a critical factor that strongly influences the shape, height, and position of the primary resonance peak. There are, of course, other reasons that the model is different from the experiment, such as the roughness of the experimental mesh surface, deviations from simple rectangular symmetry due to the lithographic production process, or variations in hole width or spacing. This work paves the way for exploration of these more detailed differences, showing how to account for the much larger effects caused by diffraction scattering and angular spread.

In simple terms, the 3D-FDTD simulations described here consist of an ultrafast pulse of light being directed at a mesh hole unit cell, with detection of the light that emerges on the other side of the mesh. The schematic shown in Fig. 2 defines the basic geometry of the simulation cell with a unit cell of the mesh at the center of the simulation region. A pulse of light with a broad band of frequencies is directed along the z -axis shown in Fig. 2 and interacts with the mesh unit cell and the periodic boundary conditions. The entire simulation region is divided into smaller rectangular regions, and finite difference forms of Maxwell's equations are solved numerically at grid points on the smaller regions. Yee's methodology [21], which calculates the electrical and magnetic fields separately using interwoven spatial grids

and alternating time steps, is used to improve convergence stability. The side boundaries of the simulation are modeled with periodic boundary conditions, with exactly one unit cell of mesh within the simulation region, so that an infinite periodic mesh is simulated. With such an arrangement, the source and detection planes are also infinite and periodic, so predictions from the simple model are understandably quite different from the results of the zero-order, low-angle experimental measurements. To improve modeling results over the simple simulation results shown in Fig. 1, a sequence of simulations were performed that effectively modeled the impact of angular spread in the incoming light. Direct "angling" of a broadband light source is not possible in FDTD models with regular periodic boundary conditions. As a substitute, within each simulation, the wave-vector component perpendicular to the mesh surface in the z - x plane (denoted " k_x ") was fixed to a particular non-zero value, and the regular periodic boundary conditions were replaced with "Bloch" boundary conditions appropriate for non-zero k_x situations. "Constant angle" data were then extracted from the "constant k_x " simulation data as described in "3D-FDTD Method." In addition, diffraction scattering information was calculated at every frequency point for each fixed k_x spectrum so that the zero-order fraction (the only light that actually enters the physical detector) could be extracted. The experimental light source in the benchtop FTIR was assumed to have maximum intensity at $\theta = 0^\circ$ (perpendicular incidence) and a Gaussian distribution of intensities about that central angle. The intensity distribution was used to weight the light transmission at each frequency or wavenumber within each calculated constant k_x spectra. The weighted spectra were then combined into a single "averaged" spectrum that could be compared with the experimental spectrum. The calculated spectrum was modeled with only one adjustable parameter, σ , which represented the standard deviation of the angle in the Gaussian intensity distribution of the FTIR spectrometer beam.

3D-FDTD Method

All calculations were performed using the commercial simulation program "FDTD Solutions 6.5" from Lumerical, Inc. (Vancouver, BC; www.lumerical.com). The simple model calculation shown in Fig. 1 (trace labeled FDTD), with light at perpendicular incidence ($k_x=0$) and no scattering calculations, required about 3 h to complete on a PC with a Microsoft Window Vista Business 64-bit operating system, an Intel[®] Core 2 Quad Processor Q9300, and 8-GB DDR2-800 RAM. Each individual fixed k_x calculation with Bloch boundary conditions and associated scattering calculations required about 8 h on the same

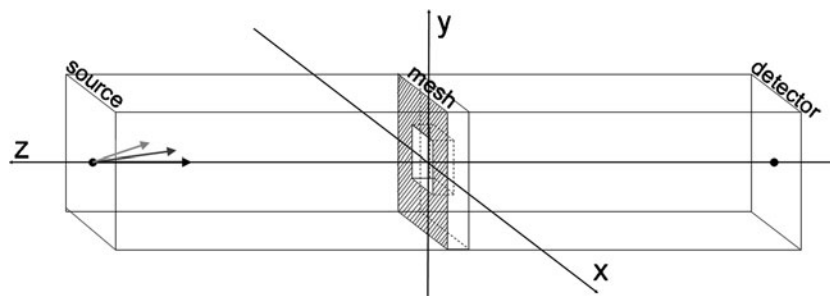


Fig. 2 Basic geometry of the simulation cell with a unit cell of the mesh at the center of the simulation region which was $12.7 \times 12.7 \times 60 \mu\text{m}$. Periodic boundary conditions simulate the periodic mesh. In the simple simulation, a pulse of light with a broad band of frequencies is directed along the z -axis, as shown with the *darkest*

arrow. In the full simulations, one effectively shoots light at the mesh at variable angles for different wavelengths by fixing k_x using Bloch boundary conditions, as schematically illustrated with the *lighter gray* arrows

system. The source, mesh, and monitors were co-planar and stretched across the short dimensions of the simulation region, with boundary conditions that made them effectively infinite. The source plane was $30 \mu\text{m}$ from the mesh, with a frequency range from 500 to $2,000 \text{ cm}^{-1}$ in 1-cm^{-1} steps. For each simulation, a plane wave of polarized light, aligned with a principal mesh axis and with an additional k_x momentum component parallel to both the electric field and the mesh surface, was propagated down the length of the simulation region. The simulation background was taken as air ($\epsilon=n=1$). The mesh was modeled as a $2\text{-}\mu\text{m}$ film of “Ni-Palik” material, perforated by a square pattern of square holes. The holes were $5.1 \times 5.1 \mu\text{m}$, with a lattice parameter of $L=12.7 \mu\text{m}$ (hole center-to-hole center distance) producing a simulation cell that was $12.7 \times 12.7 \times 60 \mu\text{m}$. The simulation region had absorbing (PML) boundary conditions (BCs) at the ends, symmetric BCs along the sides parallel to the E-field, and “Bloch” BCs along the sides perpendicular to the E-field. The symmetric BCs reduced the calculation time and memory requirements by a factor of 2 over standard periodic BCs. The Bloch BCs were used to simulate the effects of a non-zero momentum component intersecting those boundaries, which allowed the indirect calculation of the effect of light interacting with the mesh at non-perpendicular angles. To balance the competing demands of computation time and calculational accuracy, the calculation grid resolution was high (grid point-to-point distance of 10 nm) near the surface of the Ni film. It was artificially lowered (“effective index of refraction” = 1) inside the film, at depths $>50 \text{ nm}$ from the air/Ni interface, where the residual electric and magnetic fields caused by fluctuating surface waves had decayed to the point where they were negligible. The calculation time span was set to $40,000 \text{ fs}$, with a calculation step size of 0.0191 fs , for a total of about $2,094,000$ time steps per simulation. Transmission spectra were calculated at reduced (dimensionless) wavevector values of $k_x/(2\pi/L) = 0$ to 0.250 in steps of 0.005 ,

producing 51 different spectra. Every fifth spectrum (i.e., $k_x/(2\pi/L)$ steps of 0.025) is shown in Fig. 3. After each calculation, built-in “grating” functions in the FDTD 6.5 program were used to calculate the fraction of power at each frequency that scattered into each of the different diffraction spots (i.e., grating orders). The complete fraction of light that went into the $(0,0)$ diffraction grating order was assumed to enter the detector, while other higher order diffraction spots with higher scattering angles were excluded because they scattered at angles greater than the measured viewing angle of the detector window ($<10^\circ$). A grating function was calculated for each fixed k_x transmission spectrum. As with the transmission spectra, every fifth grating function (i.e., for $k_x/(2\pi/L)$ steps of 0.025) is shown in Fig. 4. The 51 different fixed k_x and corresponding grating functions constituted a set of computed “raw” data that could be combined in a weighted average to more closely match the experimental spectrum.

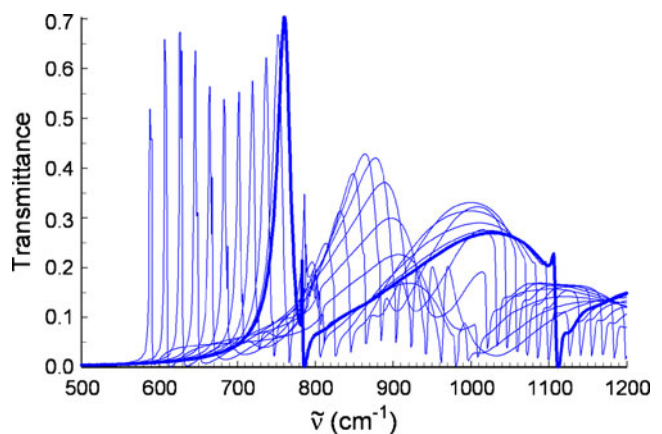


Fig. 3 Transmission spectra were calculated at reduced (dimensionless) wavevector values of $k_x/(2\pi/L) = 0$ to 0.250 in steps of 0.005 , producing 51 different spectra. Every fifth spectrum ($k_x/(2\pi/L)$ steps of 0.025) is shown above for better clarity. The $k_x/(2\pi/L) = 0$ trace is shown with a *heavier line*

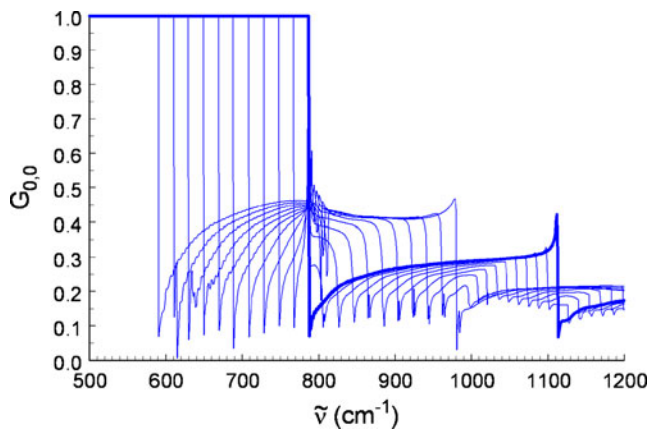


Fig. 4 Grating functions were calculated for each fixed k_x transmission spectrum. As with the transmission spectra, only every fifth grating function ($k_x/(2\pi/L)$ steps of 0.025) is shown. The $k_x/(2\pi/L) = 0$ trace is shown with a *heavier line*

Averaging Strategy for Simulation

The experimental spectrum was simulated by weighting the intensity at every frequency point $\tilde{\nu}$ in each calculated single k_x spectrum with a Gaussian weighting function $N(\tilde{\nu}, k_x, \sigma)$ defined by:

$$N(\tilde{\nu}, k_x, \sigma) = \frac{1}{\sqrt{2\pi}\sigma} e^{-\frac{1}{2}\left(\frac{\theta}{\sigma}\right)^2} \text{ where } \theta = \sin^{-1}[k_x/(\tilde{\nu}L)] \quad (1)$$

In this equation, θ is the angle of incident light as measured from the z -axis in the z - x plane (see Fig. 2) and is determined indirectly by choosing $\tilde{\nu}$ and k_x . The adjustable parameter σ represents the first standard deviation in the spread of angles of the Gaussian beam at the sample in the experimental spectrometer. Intensities at each frequency point in a particular fixed k_x spectrum were also multiplied by the zero-order grating function $G_{0,0}(\tilde{\nu}, k_x)$, which represents the fraction of transmitted light that scatters into the $(0,0)$ diffraction spot (see Fig. 4). The simulated spectrum $T'(\tilde{\nu})$ was calculated by choosing a particular value of σ and then adding up contributions from each fixed k_x spectrum $T(\tilde{\nu}, k_x)$ as weighted by angular intensity N and the zero-order grating function $G_{0,0}$:

$$T'(\tilde{\nu}_i) = \sum_j T(\tilde{\nu}_i, k_{x_j}) N(\tilde{\nu}_i, k_{x_j}, \sigma) G_{0,0}(\tilde{\nu}_i, k_{x_j}) \quad (2)$$

where j is an index over the fixed k_x spectra and i is an index over the wavenumber steps within each individual spectrum. The beam spread σ is the only adjustable parameter in this weighting calculation.

Results and Discussion

The experimental spectrum and three simulated spectra, representing σ values of 2.9° , 3.0° , and 3.1° are shown in

Fig. 5 for the range of 500 – $1,200 \text{ cm}^{-1}$. Over the entire simulation range (500 – $2,000 \text{ cm}^{-1}$), the standard deviation of comparison between the experiment and simulation of 0.0105 in transmittance occurs for $\sigma=3.0^\circ$, meaning that calculated transmittance values are within about 1% of the experimental values. As Fig. 5 shows, there is very satisfactory agreement over the majority of the spectrum between the experimental spectra and the spectra calculated using Eq. 2, i.e., weighting the calculated transmission spectra with zero-order diffraction grating functions and accounting for the angular spread of the spectrometer beam. The excellent fit between simulation and the model, using only one fitting parameter (the Gaussian beam spread σ), strongly suggests that the individual single k_x simulated spectra that were used in Eq. 2 are also generally accurate. These individual single k_x spectra come from well-defined models that are much simpler than the full experimental system, and analyzing them can shed light on the complex features of the experimental results.

For example, the experimental spectrum shows a single feature in the 780-cm^{-1} region. We have previously labeled this feature as the $(1,0)_+$ symmetric pair of the asymmetric $(1,0)_-$ primary resonance at 750 cm^{-1} , caused by front-back coupling between plasmons on opposite sides of the mesh. In the simulated spectra, this single feature separates into two clearly distinct features, one tall and sharp and the other low and broad. Analyzing the single k_x components of the simulated spectra shows that the low, broad peak centered at about 820 cm^{-1} is indeed due to the angle-shifted $(1,0)_+$ symmetric resonance, as expected. The taller, sharper peak near 785 cm^{-1} , however, does not behave like either the $(1,0)_+$ or $(1,0)_-$ peaks, which are both formed from p-polarized light. Analysis of the individual single k_x peaks, which make up the composite peak at 785 cm^{-1} ,

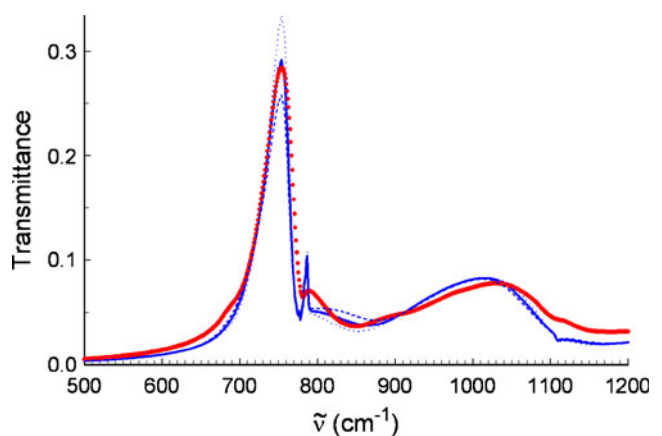


Fig. 5 Experimental spectrum (*red dots, thickest trace*) and the best-fit 3D-FDTD simulation (*solid blue trace*) with $\sigma=3.0^\circ$. Also shown are two simulations with $\sigma=2.9^\circ$ and 3.1° (*blue dotted traces*) which illustrate the sensitivity of the simulation to beam angle by bracketing the best-fit value

shows that they occur exactly where the s-polarized (0,−1) and (0,+1) peaks are predicted to occur. This result was not expected because in the simpler model, with no angular spread, the s-polarized component vanishes due to symmetry considerations.

There are several effects at play in this region of the spectrum, including splitting of resonances due to front–back coupling and the interaction between different resonances. While light consists of bosons that tend not to interact easily, surface plasmon polaritons are mixtures of light and surface waves of conducting electrons in the metal. Like electronic states of molecules, surface plasmon polaritons have some fermionic character and there are interactions between transmission resonances when light is trapped at the surface of a metal. In analyzing these possibilities, there are larger contributions to the 780-cm^{-1} region from the (0,±1) resonance than were previously appreciated.

As this case demonstrates, 3D-FDTD simulation can accurately model aspects of real, experimental systems and yield important information that helps identify and quantify surface plasmon polariton transmission resonances on metal films with arrays of subwavelength holes. Accurately capturing the angular spread of the light beam in the FTIR spectrometer required about 50 times the computational work as a simple “perpendicular incidence” simulation. However, this extra work is justified when it is important to clarify the identity and interaction of transmission resonances on the mesh.

Acknowledgments We thank the National Science Foundation for support of this work under grant nos. CHE 0848486 and CHE-0639163.

References

1. Coe JV, Heer JM, Teeters-Kennedy S, Tian H, Rodriguez KR (2008) Extraordinary transmission of metal films with arrays of subwavelength holes. *Annu Rev Phys Chem* 59:179–202
2. Coe JV, Rodriguez KR, Teeters-Kennedy S, Cilwa K, Heer J, Tian H, Williams SM (2007) Metal films with arrays of tiny holes: spectroscopy with infrared plasmonic scaffolding. *J Phys Chem C* 111:17459–17472
3. Heer J, Corwin L, Cilwa K, Malone MA, Coe JV (2010) Infrared sensitivity of plasmonic metal films with hole arrays to microspheres in and out of the holes. *J Phys Chem C* 114:520–525
4. Cilwa KE, Rodriguez KR, Heer JM, Malone MA, Corwin LD, Coe JV (2009) Propagation lengths of surface plasmon polaritons on metal films with arrays of subwavelength holes by infrared imaging spectroscopy. *J Chem Phys* 131(1):061101
5. Malone MA, Prakash S, Heer JM, Corwin LD, Cilwa KE, Coe JV (2010) Modifying infrared scattering effects of single yeast cells with plasmonic metal mesh. *J Chem Phys* 133(18):185101
6. Heer JM (2010) FDTD modeling of the spectroscopy and resonances of thin films and particles on plasmonic nickel mesh. PhD thesis, The Ohio State University, Columbus 218 pp
7. Baida FI, Van Labeke D (2002) Light transmission by subwavelength annular aperture arrays in metallic films. *Opt Commun* 209(1–3):17–22
8. Chen YG, Wang YH, Zhang Y, Lu ST (2007) Numerical investigation of the transmission enhancement through subwavelength hole array. *Opt Commun* 274(1):236–240
9. Ishihara K, Ohashi K (2005) Strong influence of surface structures on enhanced transmission through subwavelength hole arrays. *Jap J Appl Phys* 44(30):L973–L975
10. Tanaka T, Akazawa M, Sano E, Tanaka M, Miyamaru F, Hangyo M (2006) Transmission characteristics through two-dimensional periodic hole arrays perforated in perfect conductors. *Jap J Appl Phys* 45(5A):4058–4063
11. Gordon R, Hughes M, Leathem B, Kavanagh KL, Brolo AG (2005) Basis and lattice polarization mechanisms for light transmission through nanohole arrays in a metal film. *Nano Lett* 5(7):1243–1246
12. Chang S-H, Gray S, Schatz G (2005) Surface plasmon generation and light transmission by isolated nanoholes and arrays of nanoholes in thin metal films. *Opt Express* 13(8):3150
13. Chen Y, Wang Y, Zhang Y, Liu S (2007) Numerical investigation of the transmission enhancement through subwavelength hole array. *Opt Commun* 274(1):236
14. Dickson W, Wurtz GA, Evans PR, Pollard RJ, Zayats AV (2007) Electronically controlled surface plasmon dispersion and optical transmission through metallic hole arrays using liquid crystal. *Nano Lett* 8(1):281
15. Kwak E-S, Henzie J, Chang S-H, Gray SK, Schatz GC, Odom TW (2005) Surface plasmon standing waves in large-area subwavelength hole arrays. *Nano Lett* 5(10):1963
16. Laluet JY, Devaux E, Genet C, Ebbesen TW, Weeber JC, Dereux A (2007) Optimization of surface plasmons launching from subwavelength hole arrays: modelling and experiments. *Opt Express* 15(6):3488
17. Lesuffleur A, Im H, Lindquist NC, Oh S-H (2007) Periodic nanohole arrays with shape-enhanced plasmon resonance as real-time biosensors. *Appl Phys Lett* 90(24):243110
18. Rodrigo SG, Garcia-Vidal FJ, Martin-Moreno L (2008) Influence of material properties on extraordinary optical transmission through hole arrays. *Phys Rev B* 77(7):075401
19. Ruan Z, Qiu M (2006) Enhanced transmission through periodic arrays of subwavelength holes: the role of localized waveguide resonances. *Phys Rev Lett* 96(23):233901
20. Lesuffleur A, Kumar LKS, Brolo AG, Kavanagh KL, Gordon R (2007) Apex-enhanced raman spectroscopy using double-hole arrays in a gold film. *J Phys Chem C* 111:2347
21. Yee KS (1966) Numerical solution of initial boundary value problems involving Maxwell’s equations in isotropic media. *IEEE Trans on Antennas and Propagat* 14:302